ACS APPLIED MATERIALS & INTERFACES

www.acsami.org

Research Article

Achieving a Highly Stable Perovskite Photodetector with a Long Lifetime Fabricated via an All-Vacuum Deposition Process

Nurul Ridho Al Amin, Chih-Chien Lee, Yu-Chen Huang, Chun-Jen Shih, Richie Estrada, Sajal Biring, Meng-Hsueh Kuo, Chia-Feng Li, Yu-Ching Huang,* and Shun-Wei Liu*

Cite This: *ACS Appl. Mater. Interfaces* 2023, 15, 21284−21295

Read Online

ACCESS | Metrics & More | Article Recommendations | Supporting Information

ABSTRACT: Hybrid organic−inorganic metal halide perovskites (HOIP) have become a promising visible light sensing material due to their excellent optoelectronic characteristics. Despite the superiority, overcoming the stability issue for commercialization remains a challenge. Herein, an extremely stable photodetector was demonstrated and fabricated with $Cs_{0.06}FA_{0.94}Pb(I_{0.68}Br_{0.32})_3$ perovskite by an all-vacuum process. The photodetector achieves a current density up to 1.793×10^{-2} A cm^{-2} under standard one sun solar illumination while maintaining a current density as low as 8.627×10^{-10} A cm^{-2} at zero bias voltage. The linear dynamic range (LDR) and transient voltage response were found to be comparable to the silicon-based photodetector (Newport 818-SL). Most importantly, the device maintains 95% of the initial performance after 960 h of incessant exposure under one sun solar illumination. The achievements of these outstanding results contributed to the all-vacuum deposition process delivering a film with high stability and good uniformity, which in turn delays the degradation process. The degradation mechanism is further investigated by impedance spectroscopy to reveal the charge dynamics in the photodetector under different exposure times.

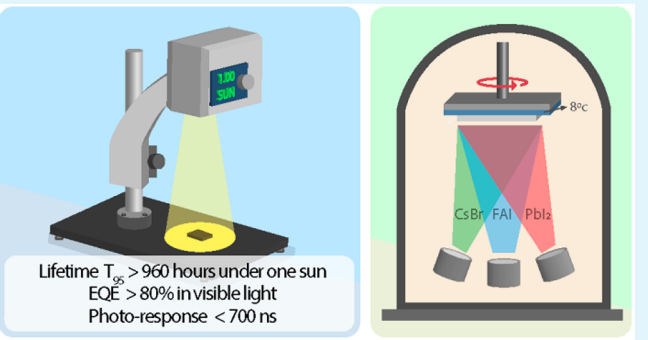

KEYWORDS: *perovskite, photodetector, stability, specific detectivity, thermal evaporation*

1. INTRODUCTION

Development of a photodetector with high performance is vital for various optoelectronic applications, including environmental surveillance, night vision, biomedical images, and optical communication.[1−4] Besides the figures-of-merit governing the performance of the photodetector such as responsivity (R), specific detectivity (D^*), and temporal response,[5−8] the operational stability of photodetector devices is a critical parameter for successful commercialization of the technology.[9−11] Conventional photodetectors are fabricated with crystalline semiconductors, predominantly silicon based due to long-term stability.[12,13] However, due to the rising cost in the fabrication processes, albeit the availability of abundant natural resources, researchers are looking for other accessible alternatives to manufacture a sensitive, low-cost, and durable photodetector.[14]

Hybrid organic−inorganic perovskites (HOIPs), an emerging crystalline semiconductor, show potential for use as a visible light photodetector due to their favorable properties such as high absorption coefficient, tunable band gap, low trap density, high charge carrier mobility, fast light responsivity, and ease of processing.[15−19] Till now, high performance perovskite-based photodetectors have been fabricated via a solution process in the laboratory.[20,21] Large-scale fabrication of the perovskite photodetector will be required for commercialization in the near future, suggesting the suitably of the thermal evaporation method. Thermal evaporation is a matured technology in industry, having unique advantages over the solution process, i.e., precise control over the film thickness, the possibility of fabricating a complex structure, and the ability to exclude the use of toxic solvents.[22−25] After the pioneering work reported by the Miyasaka group in 2009,[26] Snaith and co-workers have showcased thermally evaporated perovskite as a promising choice compared to the solution process technique.[27,28] Although progress with methylammonium lead iodide ($MAPbI_3$) is made after control over relatively high vapor pressure of methylammonium compound,[29] only limited groups could produce efficient perovskite solar cells surpassing a power conversion efficiency (PCE) of 20.0% based on thermal evaporation process.[30] In 2018, Li et al. have realized perovskite mini-modules on an

Received: January 18, 2023
Accepted: April 7, 2023
Published: April 20, 2023

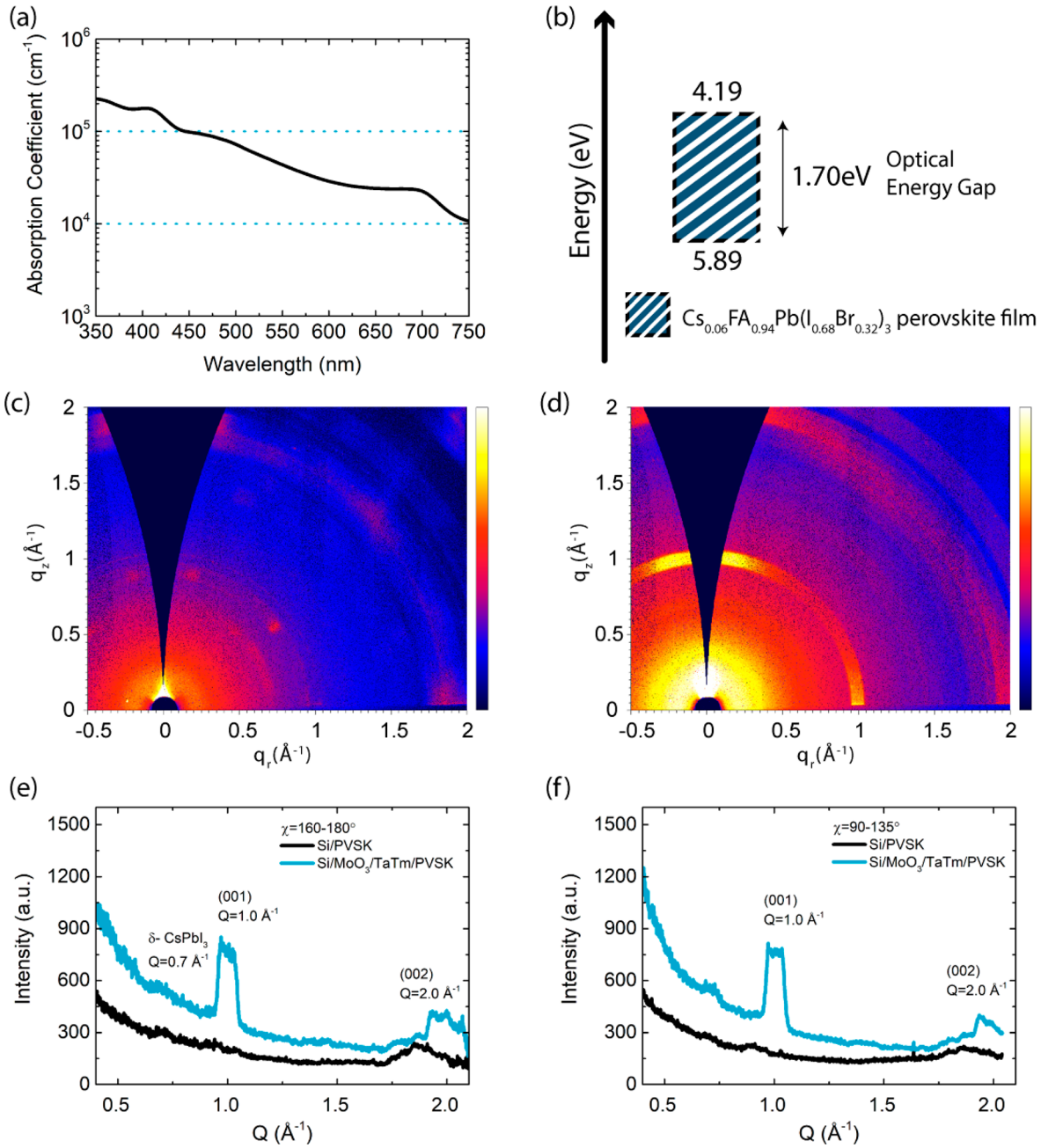

Figure 1. (a) Perovskite thin film characterization. (a) Absorption spectrum. (b) The energy level of CsFAPbIBr. Two-dimensional GIWAXS patterns corresponding to the vacuum-deposited CsFAPbIBr films prepared with different substrates: (c) Si/PVSK, (d) Si/MoO_3/TaTm/PVSK, (e) in-plane, (f) out-of-plane.

active area of 21 cm^2 with PCE up to 18.13%.[31] This validates the possibility of large-area mass production via thermal deposition of perovskites. However, limited success is achieved in thermal evaporation of perovskites rather than a methylammonium system. Besides, the ambiguity on the long-term stability of the methylammonium-based perovskite has rarely been addressed for devices fabricated via a thermal evaporation process.

The volatility and decomposition of the methylammonium cation under thermal stress hinder the long-term stability of the methylammonium-based perovskite optoelectronics. In 2017, Borchert and co-workers explored the potential of formamidinium lead iodide perovskite ($FAPbI_3$) as an alternative for a large-area solar cell system under vacuum deposition. The compact, pinhole-free, homogeneous thin film of $FAPbI_3$ with large-area (8 × 8 cm^2) demonstrates the potential of the formamidinium compound as a vapor deposited alternative instead of the $MAPbI_3$ system. However, the $FAPbI_3$ perovskite suffers from an undesirable non-perovskite phase (δ-phase) with yellow color under high humidity with limited device performance.[32] Utilization of additives to stabilize the crystal phase by controlling crystal growth has resulted in the smoother morphology of the perovskite film with passivated defects and improved device performance.[33] Yi et al. demonstrated that adding CsI to $FAPbI_3$ stabilizes the crystal phase and eliminates the undesirable δ-phase, while adding CsBr to $FAPbI_3$ achieves the highest performance out of three proposed compositions

https://doi.org/10.1021/acsami.3c00839
ACS Appl. Mater. Interfaces 2023, 15, 21284−21295

using a solution process method. This mixed $Cs_xFA_{(1-x)}PbX_3$ device also shows a good stability of 1000 h stored in the dark under ambient condition and without encapsulation.[34] Further investigation by Liu et al. shows that incorporating CsI or CsBr additive into $FAPbI_3(Cl)$ using a solution process not only avoids the undesirable δ-phase but also improves the film quality, maintains the stability, balances the charge mobility, and reduces the trap states.[35] In 2020, Chiang et al. demonstrated the feasibility of a three-source vacuum deposition process for $FA_{0.7}Cs_{0.3}Pb(I_{0.9}Br_{0.1})_3$ perovskite thin films to avoid the formation of undesirable δ-phase and achieve PCE values up to 18% and J_{sc} up to 23 mA cm^{-2} by adding excess PbI_2 in the methylammonium-free thin film. The encapsulated device shows no degradation in performance for 18 days under ambient conditions.[24]

In this work, we optimize a perovskite photodetector using CsBr, FAI, and PbI_2 materials under a fully thermal vacuum deposition process. The optimized perovskite device is then compared to the commercially available (Newport 818-SL) silicon-based photodetector (Si−Pd). Our optimized device achieves J_{sc} of 1.793×10^{-2} A cm^{-2}, J_{dark} of 8.627×10^{-10} A cm^{-2} at zero bias voltage, and a high on/off ratio of 2.08×10^7. The device also shows a long linear dynamic range (LDR) and a fast photovoltage response comparable to that of the Newport 818-SL Si−Pd. To test the stability of the perovskite material, the thin film was stored at 25 °C and at relative humidity of 30% in dark conditions. Similarly, the device stability was studied by exposing the device under one sun illumination with different exposure times in ambient conditions. We find that our optimized perovskite device is able to maintain 95% of the initial performance after even 960 h in ambient environment. The dark current of the perovskite device is stable even after running forward and reverse scans continuously 1000 times. This exceptional stability is explained well using GIXRD data. In addition, impedance spectroscopy is employed to reveal the charge dynamics of the photodetector under different exposure times to understand the degradation mechanism process.

2. RESULTS AND DISCUSSION

The absorption coefficient of the CsFAPbIBr perovskite film deposited directly on the glass substrate is shown in Figure 1a. The absorption coefficient is over 10^4 cm^{-1} in the wavelength range of 350−750 nm, suggesting the application of the perovskite material in the visible wavelength. The valence band (VB) of the perovskite film is determined by using ultraviolet photoelectron spectroscopy (UPS) with an ionization source of He I (21.2 eV). From the UPS spectrum shown in Figure S1, the work function and highest occupied molecular orbital (HOMO) of the CsFAPbIBr perovskite film is estimated to be −3.89 and −5.89 eV, respectively. An optical energy gap of about 1.7 eV is obtained from the UV absorption spectrum. Therefore, the lowest unoccupied molecular orbital (LUMO) of the perovskite film is −4.19 eV. The energy levels of the CsFAPbIBr perovskite film is shown in Figure 1(b). We elucidate the chemical composition of the perovskite film by X-ray photoelectron spectroscopy (XPS). The XPS signals of Cs 3d, N 1s, I 3d, and Br 3d are detected. The XPS spectra of Cs 3d, N 1s, I 3d, and Br 3d are processed by XPSPEAK software, and the relative amounts of the constituent atoms of the CsFAPbIBr perovskite films are summarized in Table S1. The XPS spectra of CsFAPbIBr perovskite films is shown in Figure S1c. The atomic ratios of Cs:N and Br:I are 0.06 and 0.46, respectively, as calculated by integrating the area under the peak corresponding to the elements. Therefore, the chemical composition of the perovskite films can be determined as $Cs_{0.06}FA_{0.94}Pb(I_{0.68}Br_{0.32})_3$.

The grazing incidence small-angle X-ray scattering (GI-SAXS) results shown in Figure S1d and e indicate that the perovskite deposited directly on silicon (Si) substrate exhibits nanocrystal domains ($Q \sim 0.025$ $Å^{-1}$), while the perovskite deposited on the TaTm film shows larger crystal domains with dense perovskite grains or no micropore inside the perovskite film. The GISAXS profiles were obtained by cutting a horizontal line (in-plane direction) around the Yoneda peak of the active layer on the 2D GISAXS patterns.[36,37] Figure 1c−f present the 2D grazing incidence wide-angle X-ray scattering (GIWAXS) patterns which shows the diffraction rings corresponding to the (001) and (002) planes at Q = 1 and 2 $Å^{-1}$, respectively. The wedge-shaped area of pole figures is related to the contribution of crystallites at exactly out-of-plane direction (Q_x = 0) which could be missed. The literature proposes a line-cut approach to correct the wedge-shaped area by Gaussian fitting.[37−39] In the present work, we consider all other oriented crystallites around the out-of-plane direction to represent all crystallites over this azimuthal distribution so that the correction to the wedge-shaped area is not adopted. This approximation is available for the qualitative and relative interpretation. For the perovskite deposited on the TaTm film (PVSK/TaTm), the (001) plane oriented to the out-of-plane direction (Q_z direction), i.e., perpendicular to the TaTm film surface dominates. In comparison to the perovskite deposited on the Si, the clear diffraction spot in the Q_z direction of PVSK/TaTm films indicates the highly oriented crystallites. In addition, the PVSK/TaTm shows that a fraction of crystallites exhibiting the (001) plane oriented to the in-plance direction (Q_x direction), i.e., parallel to the TaTm film surface. We can determine the relative crystallinity according to the azimuthally integrated intensity of the (001) ring in the 2D GIWAXS pattern (polar angle (χ): 90−180°). Based on our previous study,[40] the relative crystallinity can be roughly determined from the integration of peak intensities. The PVSK/TaTm reveals a higher crystallinity along the Q_z direction than the perovskite films on the Si. Moreover, the appearance of diffraction spot at Q = 0.7 $Å^{-1}$ in the perovskite deposited on the Si implies the presence of nonperovskite phase (δ-$CsPbI_3$ crystallites) in the perovskite film, which is spontaneously converted from the perovskite phase. δ-$CsPbI_3$ has been confirmed in the previous research.[41] However, the PVSK/TaTm film shows a large number of perovskite crystallites oriented along Qz-direction and absence of the δ-$CsPbI_3$ crystallites. The determination of orientation distribution of the edge-on crystallites as the majority was obtained by azimuthal distribution along (χ): 40−150° according to the azimuthal-tube-cut method.[42] The fwhm ($\sim 2.35\sigma$) values of the edge-on crystallites for the Si/PVSK and Si/MoO_3/TaTm/PVSK films are 35° and 23°, respectively.

The contribution of isotropic crystallites around the (100) arc spot can be ignored. According to our results, Si/MoO_3/TaTm/PVSK film shows a large amount of Q_z crystallite orientation and no nonperovskite phase (δ-CsPbI3 crystallites). Therefore, we believe that the high Qz crystallite orientation facilitates the carrier transport in the vertical direction and the regular lattice arrangement is benefited to reduce the defects and avoid structural degradation due to water penetration. This is the main reason for the good

https://doi.org/10.1021/acsami.3c00839
ACS Appl. Mater. Interfaces 2023, 15, 21284−21295

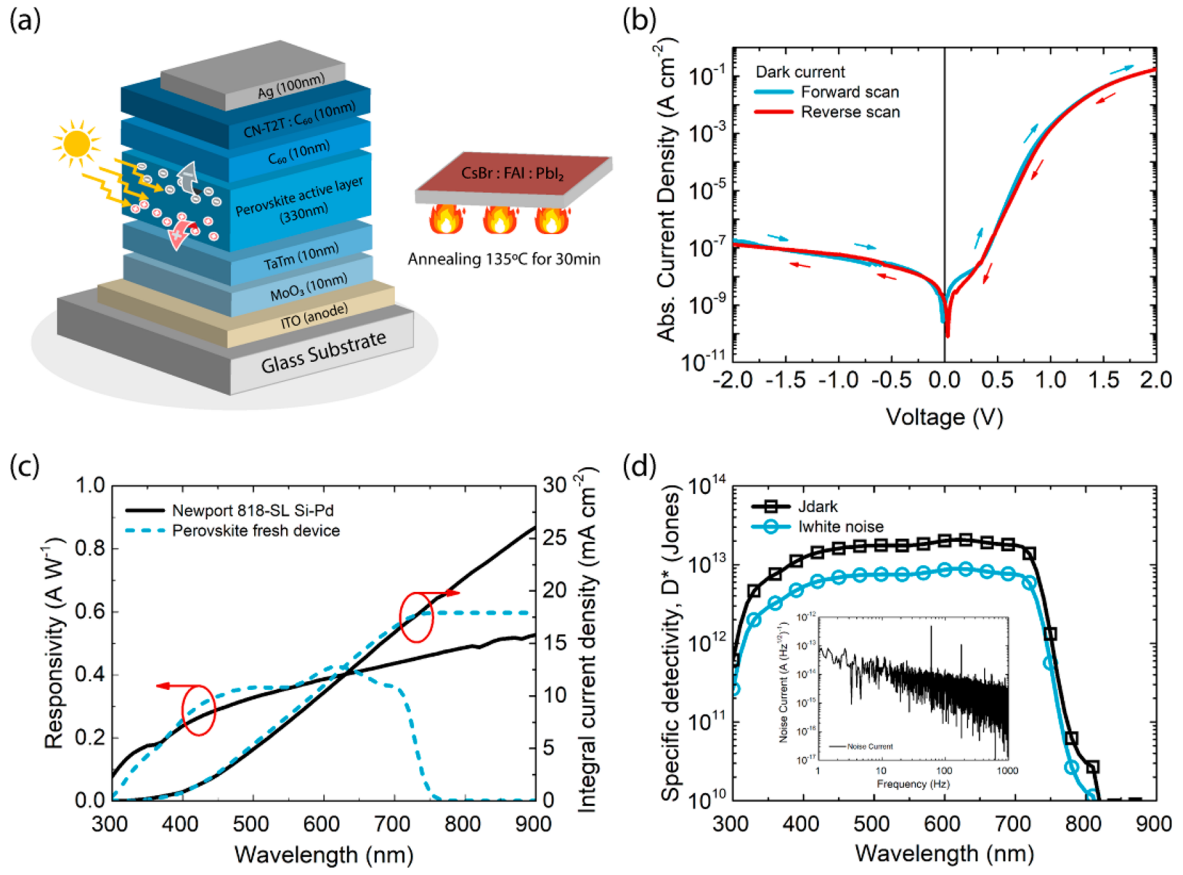

Figure 2. (a) The perovskite device structure. (b) $J-V$ curves. (c) Responsivity (A/W) spectra and integrated current density of the perovskite device compared to Newport 818-SL silicon photodetector. (d) Specific detectivity (D^*) under dark conditions, inset incudes the noise current.

performance and high stability of the perovskite photodetector fabricated by thermal vacuum deposition.

The optimized structure of our perovskite device is shown in Figure 2a. The structure follows as ITO/MoO_3 (10 nm)/TaTm (10 nm)/$Cs_{0.06}FA_{0.94}Pb(I_{0.68}Br_{0.32})_3$ (330 nm)/C_{60} (10 nm)/CN-T2T:C_{60} (10 nm)/Ag (100 nm). The substrate temperature was controlled at 8 °C with an annealing temperature set at 135 °C for 30 min. The detailed performances are summarized in Table S2. The device with optimized perovskite and structure exhibits an open-circuit voltage (V_{oc}) of 0.98 V, J_{sc} of 1.793×10^{-2} A cm^{-2}, J_{dark} of 8.627×10^{-10} A cm^{-2}, and a light on/off ratio of 2.08×10^7 at zero bias voltage. Figure 2b depicts the $J-V$ curve under forward and reverse bias from −2.0 to 2.0 V. We observe hysteresis as the forward J_{dark} of 8.627×10^{-10} A cm^{-2} and reverse J_{dark} of 1.265×10^{-9} A cm^{-2} at zero bias voltage. Figure S2a shows the external quantum efficiency (EQE) spectra. The EQE spectra of the perovskite device at zero bias voltage show broadband spectrum under visible wavelength covering the range from 300 to 780 nm with two main peaks at 470 and 610 nm, while the Si−Pd shows a larger broadband with the response beyond 780 nm. The high EQE value over 80% is correlated to the high absorption coefficient at the specific wavelength. The responsivity and integral current density under zero bias voltage for perovskite devices compared to Si−Pd are shown in Figure 2c. The responsivity of the perovskite device surpasses that of Si−Pd in the range of 390−640 nm, showing the superiority of our perovskite device as an application in the visible wavelengths. The responsivity of perovskite device at zero bias voltage at the wavelength of 530 nm is 0.359 A W^{-1}, slightly higher than that (0.346 A W^{-1}) of Si−Pd one. The specific detectivity (D^*) is an important parameter of a photodetector because determines the detection ability at the weakest photo signal. Figure 2d shows the D^* obtained using J_{dark} and $I_{white\ noise}$ as expressed in eqs 1 and 2 given below

$$D^* = \frac{R}{\sqrt{2qJ_{dark}}} \tag{1}$$

$$D^* = \frac{R\sqrt{A\Delta f}}{I_{white\ noise}} \tag{2}$$

where R is responsivity (A W^{-1}), q is elementary charge (1.602×10^{-19} C), J_{dark} is dark current density (A cm^{-2}), A is the area (cm^{-2}), Δf is noise bandwidth (Hz), $I_{white\ noise}$ is the root-mean-square (RMS) of white noise current (A). The D^* values for both J_{dark} and $I_{white\ noise}$ are over 10^{12} Jones in the wavelength range of 350−700 nm, while 1.747×10^{13} for J_{dark} and 7.496×10^{12} for $I_{white\ noise}$ at the wavelength of 530 nm. The D^* value is measured under zero bias voltage and noise current spectra is shown in the inset of the figure. The value of $I_{whitenoise}$ was obtained using eq 3[43]

$$I_{white\ noise} = \sqrt{\int_{f_1}^{f_2} {i_n}^2 \mathrm{d}f} \tag{3}$$

where f_1 is lower and f_2 is higher bandwidth (Hz) and ${i_n}^2$ is the noise current value (A (Hz$^{1/2}$)$^{-1}$). The $I_{whitenoise}$ value was 2.98×10^{-15} A at the bandwidth range from f_1 = 100 Hz to f_2 =

https://doi.org/10.1021/acsami.3c00839
ACS Appl. Mater. Interfaces 2023, 15, 21284−21295

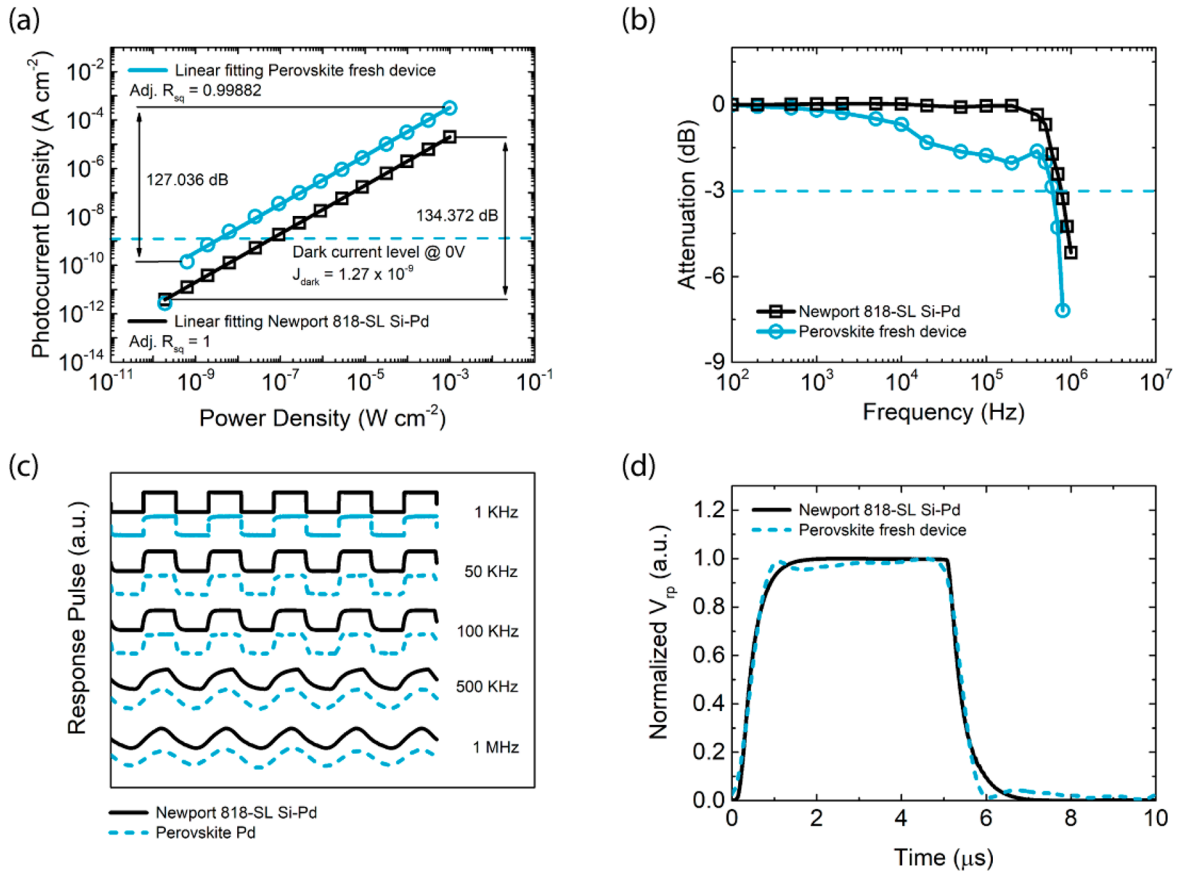

Figure 3. Pristine perovskite device compared to the Newport 818-SL silicon photodetector. (a) The linear dynamic range (LDR) and (b) the attenuation (dB) at a cutoff frequency −3 dB of the perovskite device under green LED illumination at 525 nm. (c) The pulse response under different given frequencies of 1 kHz, 50 kHz, 100 kHz, 500 kHz, and 1 MHz. (d) The photovoltage response of the perovskite device at zero bias voltage and frequency of 100 kHz under green LED illumination at 525 nm.

1000 Hz. The linearity of the response at different light intensities is also investigated. The linear dynamic range (LDR) of the devices, i.e., the ratio between the current densities at higher and lower intensity of the light while maintaining the linear response is measured. A photodetector with wider LDR provide the opportunity to sense light with wider variation in intensities linearly. The LDR is calculated following the equation given as

$$\mathrm{LDR} = 20 \log\left(\frac{J_{\mathrm{high}}}{J_{\mathrm{low}}}\right) \tag{4}$$

where J_{high} is the higher limit and J_{low} is the lower limit of current density (A cm^{-2}) under light exposure. Figure 3a compares the LDR plot of our perovskite device and Si−Pd at zero bias with green light emitting diode (LED) at wavelength of 530 nm as the light source. Our perovskite device shows LDR of 127.036 dB with J_{dark} of 1.27×10^{-9} A cm^{-2} at zero bias voltage. The LDR (134.372 dB) of Si−Pd is slightly higher resulted from low J_{dark} (3.83×10^{-12} A cm^{-2}). The two order of difference in LDR is derived from the limitation of achieving the dark current in our device below 1.41×10^{-10} A cm^{-2}. In addition, the frequency response (known as $f_{-3\ \mathrm{dB}}$) is presented for further investigation. Here, the bandwidth of $f_{-3\ \mathrm{dB}}$ describes the attenuation factor, expressing the output optical signal degraded by $1/\sqrt{2}$ according to an input of the illumination power density.[44−47] The attenuation (dB) at a cutoff frequency of −3 dB is shown in Figure 3b. The cutoff frequencies (at −3 dB) of the perovskite and Si−Pd devices are around 600 kHz and 700 kHz, respectively. The attenuation of the perovskite device at 1 kHz degrades around −0.18 dB. The Si−Pd maintains the frequency response until around 400 kHz with attenuation degrading around −0.35 dB. For further investigation, the pulse response is measured under different given frequencies at 1 kHz, 50 kHz, 100 kHz, 500 kHz, and 1 MHz for both the perovskite and Si−Pd devices.

Figure 3c shows the response of the perovskite device comparable to Si−Pd. Above the given frequency of 500 kHz, both the devices show sinusoidal response since the applied frequency is above the cutoff frequency. As the photodetector needs to have a fast response, it is important to investigate the response time. Two parameters can be extracted from the response time which are rise time (τ_{rise}) and fall time (τ_{fall}). The response time is correlated to charge recombination, transportation, and collection processes. The time taken for photovoltage to rise from 10% to 90% is defined as the τ_{rise} and to drop from 90% to 10% is defined as the τ_{fall}. Figure 3d shows the photovoltage response of the perovskite device, which is measured using green LED at wavelength of 525 nm under zero bias voltage and 100 kHz frequency. The perovskite device shows the τ_{rise} of 629.6 ns and the τ_{fall} of 616.6 ns, while the Si−Pd shows the τ_{rise} of 694.4 ns and the τ_{fall} of 830.5 ns. We observe that the response time of our perovskite the τ_{fall} of 19.5 μs.[48] It insinuates the possibility of introducing CsBr material into the $FAPbI_3$ system to reduce carrier trapping and improve the grain quality, resulting in a faster response time in

https://doi.org/10.1021/acsami.3c00839
ACS Appl. Mater. Interfaces 2023, 15, 21284−21295

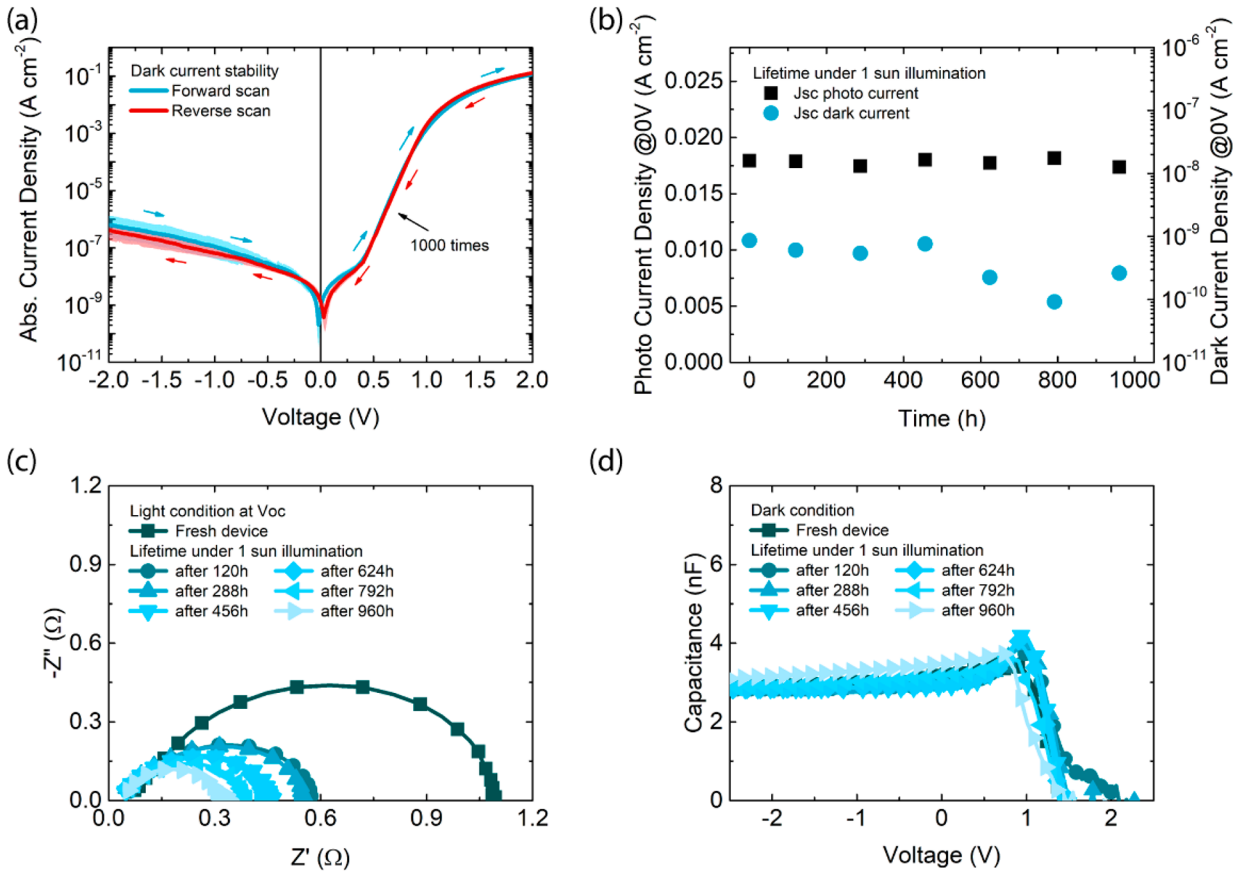

Figure 4. (a) The dark current stability of the perovskite device after continuous forward and reverse scans for 1000 times. (b) The light and dark current density value at zero bias voltage after being exposed under one sun illumination for different exposure times. (c) Complex impedance plot of the perovskite device under light conditions. (d) Capacitance−voltage ($C-V$) of the perovskite device under dark conditions.

the photodetector. The uniform and pinhole-free film is desirable for a smoother junction to achieve an efficient photodetector with a high-speed response. To test the device lifetime and stability, we measure the performance of the perovskite device under one sun illumination for different exposure times at ambient atmosphere. The EQE spectra, responsivity, and integral current density are shown in Figure S2. The lifetime data of the perovskite device are summarized in Table S2. As we know several factors could affect the degradation such as moisture, oxygen, and heat. We believe that the low degradation observed in the perovskite device is due to good encapsulation which could avoid moisture and oxygen. The data also show that the EQE value is still maintained at over 80% after being exposed to one sun for 960 h. This indicates excellent photon-to-electron conversion efficiency as well as high absorption coefficient value. The overall device performance is still maintained at over 95% even after 960 h exposure under one sun illumination. Figure S3 shows the forward and reverse scan of the $J-V$ curve under light and dark conditions after being exposed to one sun illumination. The differences between $J-V$ curves, which mostly appears near open-circuit conditions, can be described using the modified hysteresis index (HI) eq 5, as given below[49]

$$\mathrm{HI} = \frac{J_{\mathrm{reverse}}(0.8V_{\mathrm{oc}}) - J_{\mathrm{forward}}(0.8V_{\mathrm{oc}})}{J_{\mathrm{reverse}}(0.8V_{\mathrm{oc}})} \quad (5)$$

where $J_{\mathrm{reverse}}(0.8\ V_{\mathrm{oc}})$ and $J_{\mathrm{forward}}(0.8_{\mathrm{Voc}})$ are the photo current density at 80% of V_{oc} for reverse and forward scans, respectively. Equation 5 was modified based on the HI from Sanchez et al.,[50] where regardless how the HI is defined, the value still could differentiate the type of hysteresis.[51,52] The normal hysteresis is the condition when the forward scan data is lower than the reverse scan data, where the vice versa, shows the inverted hysteresis. The normal hysteresis shows positive HI value and inverted hysteresis marked by negative HI value. Table S3 shows the HI of the perovskite device for different exposure times. The HI value is lower than 0.05, where the fresh device shows values of 0.0165 and 0.0289 after 960 h. This HI value indicates low normal hysteresis resulting from appropriate perovskite composition achieving better charge balance.

To verify the device stability, we test the lifetime of the perovskite film by keeping it in the dark condition inside the humidity-controlled dry cabinet at a temperature of 25 °C, and the humidity level set to 30%. The change in absorption coefficient, X-ray diffraction (XRD), and surface roughness were monitored for several days. Figure S4a results show that the absorption coefficient decreases over time while still maintaining a high value over 10^{-4} even after 30 days of storage. The decay observed in perovskite film is caused by humidity. The absorption spectra indicate that the film remain still in the perovskite phase even after 30 days of storage. Figure S4b shows that the XRD pattern of the perovskite film exhibits two strong peaks, which represent the (001) plane at 14.12° and the (002) plane at 28.39°, respectively. The XRD pattern of the films did not change after 5 days, indicating that the film crystallinity and perovskite phase composition

https://doi.org/10.1021/acsami.3c00839
ACS Appl. Mater. Interfaces 2023, 15, 21284−21295

Table 1. Performance Comparison of Formamidinium (FA) Based Perovskite Photodetectors

Active materials	Fabrication method	Active wavelength (nm)	On/off ratio	Responsivity (A W^{-1})	Detectivity (Jones)	LDR (dB)	−3 dB	τ_{rise}/τ_{fall}	Stability (days)	Ref
$Cs_{0.06}FA_{0.94}Pb(I_{0.68}Br_{0.32})_3$	thermal vapor deposition	300−780	2.08×10^7	0.359 (0 V @ 530 nm)	1.747×10^{13} (0 V @ 530 nm)	127	600 kHz	629/616 ns	40 (device)[a] 30 (thin film)[b]	This work
$FAPbI_3$	doctor-blading deposition	-	10^5	11.46 (10 V @ 532 nm)	-	-	-	5.4/10.9 ms	-	53
$FAPbI_3$	modified inverse temperature crystallization	-	-	0.68 (0.1 V @ 380 nm)	-	-	-	12.4/17.2 ms	-	54
$FAPbI_3$	solution process	330−800	4.5×10^4	0.95 (−1 V @ 650 nm)	2.8×10^{12} (−1 V @ 650 nm)	92	215 kHz	7.2/19.5 μs	-	48
$FAPbI_3$	solution process	300−850	-	-	3.8×10^{12} (0 V @ 800 nm)	148	1.2 MHz	6.8/3.9 ns	-	55
1D $FAPbI_3$:10 mol % PEA^+	asymmetric wettability topographical template	-	-	5.282×10^3 (5 V @ 630 nm)	1.45×10^{14} (5 V @ 630 nm)	-	15 kHz	29.3/31.1 μs	28 (thin film)[c]	56
2D $FAPbI_3$	ligand-assisted reprecipitation method	300−815	1.4×10^3	3.27 (9 V @ 645 nm)	1.35×10^{12} (3 V @ 645 nm)	-	-	0.35/0.54 ms	-	57
2D (OA) $2FA_{n-1}Pb_nBr_{3n+1}$	solution process	350−580	-	32 (9 V @ 442 nm)	-	-	-	0.25/1.45 ms	-	58
$FAPbBr_3$	modified inverse temperature crystallization	-	-	4×10^4 (5 V @ 495 nm)	3.87×10^{14} (5 V @ 495 nm)	-	-	0.67/0.75 ms	-	59
$FAPbBr_3$ QDs/graphene	reprecipitation method	-	-	1.15×10^5 (2 V @ 520 nm)	-	-	-	58/60 ms	-	60
$Cs_{0.15}FA_{0.85}PbI_3$	solution process	240−750	6.3×10^3	5.7	2.7×10^{13}	76.3	3.8 MHz	45/91 ns	45 (device)[d]	61
$Cs_{0.1}FA_{0.9}PbI_3$	solution process	300−850	-	0.762 (−5 V @ 520 nm)	5.08×10^{13} (−0.5 V @ 520 nm)	94	-	59.25/53.85 μs	30 (device)[e]	62
$PtSe_2$/ $Cs_{0.15}FA_{0.85}PbI_3$	solution process	300−1200	5.7×10^3	117.7 (0 V @ 808 nm)	2.91×10^{12} (0 V @ 808 nm)		2 MHz	78/60 ns	21 (device)[r]	63
$PdSe_2$/ $Cs_{0.15}FA_{0.85}PbI_3$	solution process	200−1200	6.46×10^4	0.313	2.72×10^{13}		20.1 kHz	3.5/4 μs	-	64
$Cs_{0.3}FA_{0.7}Pb(I_{0.8}Br_{0.2})_3$	solution process	300−750	3.4×10^5	1.1 (1 V @ 450 nm)	2.8×10^{13} (1 V @ 450 nm)	120		0.11/0.35 ms	90 (device)[d]	65
$MA_{0.7}FA_{0.3}PbBr_3$	solution process	-	10^5	0.51	4×10^{12}	100		6.7/2.5 ms	90 (device)[d]	66
$(Cs_{0.05}(FA_{0.83}MA_{0.17})_{0.95})Pb(I_{0.9}Br_{0.1})_3$	solution process	300−810	7.3×10^5	0.52 (0 V)	8.8×10^{12} (0 V)			19/21 μs	-	67
$(FASnI_3)_{0.6}(MAPbI_3)_{0.4}$	solution process	300−1000	-	0.4 (−0.2 V @ 900 nm)	1.1×10^{12} (−0.2 V @ 900 nm)	167		6.9/9.1 μs	90 (device)[g]	68
$(BA)_2FAPb_2I_7$:FACl	solution process			2.3 (2 V @ 405 nm)	3.2×10^{12} (2 V @ 405 nm)	93		9.74/8.91 μs	41 (device)[f]	69

[a]Exposed under one sun illumination at room temperature conditions. [b]Storage in ambient conditions with a relative humidity of 30% at 25 °C. [c]Storage in ambient conditions with a relative humidity of 50 ± 2% at 25 ± 2 °C. [d]Storage in ambient conditions. [e]Stored in an ambient conditions with relative humidity of 35−60% without encapsulation and wrapped in aluminum foil under dark conditions. [f]Storage in ambient conditions without encapsulation. [g]Sstorage in a N_2-filled glovebox without any encapsulation.

https://doi.org/10.1021/acsami.3c00839
ACS Appl. Mater. Interfaces 2023, 15, 21284−21295

unchanged. Figure S4c−e show the surface morphology of perovskite film acquired by AFM. The 2D AFM image is taken over 5 μm × 5 μm size of the pristine perovskite film showing an average roughness (R_{rms}) around 24.5 nm. This value is similar to that (~26.6 nm) of $Cs_xFA_{1-x}PbI_{3-x}Br_x$(Cl)-based perovskite films produced by other method.[35] We also find that the perovskite film evaporated using the thermal vacuum deposition process is homogeneous, uniform, and pinhole-free. The R_{rms} value of the pristine film decreases from 24.5 to 22.0 nm after 2 days and finally, to 19.9 nm after 30 days. Kato et al. have reported the R_{rms} values of α-$FAPbI_3$ and δ-$FAPbI_3$ as 10.9 and 5.7 nm, respectively.[70] Again, the decrease in R_{rms} value is caused by humidity. As the crystal structure and morphology affect the device performance, the small change in morphology of our perovskite thin film could preserve the crystal structure and slow down the degradation process in the device. These outstanding performances are resulted from the high stability and good uniformity of the film fabricated by using a thermal vacuum deposition process. The slow degradation process is achieved by introducing CsBr material into $FAPbI_3$.[71] We also investigated the stability of the dark current after 1000 cycles of continuous forward and reverse scans. The average data is plotted in Figure 4a. Note that the normal hysteresis and the data are quite stable even after 1000 cycles of continuous forward and reverse scans. We believe that this stability is achieved by having an appropriate perovskite composition, carefully designing the device structure, and good cell encapsulation, as well as having uniformity of perovskite film. All of these benefits are accomplished using thermal vacuum deposition process. The change in current density in dark and under one sun illumination for different exposure times is plotted in Figure 4b. We observe that the J_{sc} and J_{dark} are quite stable even at the increased exposure time. Impedance spectroscopy is, in general, applied to understand the degradation mechanism as well as charge dynamics and charge accumulation.[72−76] This measurement is employed in this study to explain the lifetime issue of the perovskite device before and after continuous exposure of one sun illumination with different exposure times. The complex impedance plot under light illumination is shown in Figure 4c. Two parameters could be identified from the complex impedance such as the high-frequency region (>1 kHz), and low-frequency region (<1 Hz). Here, the complex impedance is measured by sweeping the frequency from 1 Hz to 1 MHz. The semicircle from complex impedance data at high frequency is related to the charge transport and dielectric response.[74] Note that the change in capacitance at the high-frequency region is related to geometric capacitance (C_{geo}). The data appear as semicircles with a decrease in diameter as the exposure time increases. The decrease in diameter becomes negligible below 1 Ω, suggesting a stable device. The small decrease in diameter indicates a slight change in the dielectric response of the perovskite layer over time. A $C-V$ measurement is carried out for analyzing the charge dynamics and charge accumulation as the charge accumulation is a critical factor affecting the hysteresis. The $C-V$ measurement for the perovskite device under dark conditions is shown in Figure 4d. Two distinct regions could be observed in the plot, which are the plateau region (corresponding to C_{geo}) and the $C-V$ peak region (corresponding to charge accumulation). The plateau region could be related to the dielectric response of the perovskite layer, where at the $C-V$ peak region, the increase of the capacitance value resulted from charge accumulation at the perovskite interface. The high charge accumulation could be an indication of charge imbalance between electron and hole. The data shows that the perovskite device accumulates less charge. As the degradation starts, the capacitance decreases, indicating the reduction in charge accumulation and faster charge recombination. We suggest that the property of the material in the device changes during the degradation process. The increase in C_{geo} may be attributed to the increase in leakage charge. At the end of discussion, we compare the device performance covering active-wavelength, on/off ratio, responsivity, detectivity, LDR, −3 dB, response time, and stability of formamidinium (FA) based perovskite photodetector ever published in Table 1. The most common fabrication method used is the solution process. Therefore, an FA-based perovskite photodetector fabricated specifically by thermal vapor deposition is hard to find. Our device performance also shows a high on/off ratio and fast response at nanosecond. The responsivity and detectivity are comparable with other FA-based perovskite photodetector with different fabrication methods. Furthermore, we demonstrate good stability of the perovskite film as well as photodetector. We examine the stability of our perovskite device by exposing it under one sun LED solar simulator at room temperature, where the stability has mostly been studied (by other groups) by storing the device under ambient or dark conditions. This exceptional stability shows the potential of device fabrication using thermal vacuum deposition.

3. CONCLUSION

We have optimized a perovskite photodetector using a codeposition process for CsBr, FAI, and PbI_2 materials under a fully thermal vacuum condition. The device shows a lower J_{dark} of 8.627×10^{-10} A cm^{-2} at zero bias voltage and the response time similar to that of a commercial Si−Pd based photodetector. Materials characterizations reveal stable, uniform, and pinhole-free perovskite film fabricated by using thermal vacuum deposition, slowing down the degradation process. The perovskite device maintains 95% of the initial performance after being exposed under one sun illumination for a 960 h lifetime. Finally, impedance spectroscopy is employed to analyze the charge dynamics of the photodetector under different exposure times, which helps us to understand the degradation mechanism in detail.

4. EXPERIMENTAL SECTION

In this study, the perovskite device was fabricated using a commercial indium-tin-oxide (ITO) coated glass substrate (15 Ω/sq) purchased from Luminescence Technology while the perovskite film was deposited onto the glass substrates and the silicon substrate. All the substrates were cleaned using dish soap and afterward sequentially soaked in the deionized (DI) water, acetone, and isopropyl alcohol (IPA) in a sonication bath within 10 min, and then dried using a nitrogen gas blower. For the materials, N4,N4,N4″,N4″-tetra([1,1′-biphenyl]-4-yl)-[1,1′:4′,1″-terphenyl]-4,4″-diamine (TaTm, > 99%) was purchased from Shine Material Technology and 3′,3‴,3⁗,3⁗⁗-(1,3,5-triazine-2,4,6-triyl)tris(([1,1′-biphenyl]-3-carbonitrile)) (CN-T2T, > 99%) was purchased from Unichem Technology. The buckminsterfullerene (C_{60}, > 99.9%) was purchased from Luminescence Technology and formamidinium iodide (FAI, > 99.99%) was purchased from Greatcell Solar Material. The molybdenum trioxide (MoO_3, > 99.9995%) and cesium bromide (CsBr, > 99.999%) were purchased from Alfa Aesar, and lead(II) iodide (PbI_2, > 99.999%) was purchased from Sigma-Aldrich. All the materials were used directly after purchased without further purification process. The perovskite

https://doi.org/10.1021/acsami.3c00839
ACS Appl. Mater. Interfaces 2023, 15, 21284−21295

device and film were fabricated using a thermal evaporation system under a vacuum level of ~2×10^{-6} Torr and the deposition rate was controlled at around 0.5−1 Å s^{-1} (except for silver, the deposition rate using 3 Å s^{-1}). In the fabrication of the perovskite active layer, the deposition rate of CsBr, FAI, and PbI_2 was deposited with rates of 0.6, 0.9, and 0.6, where the temperature of FAI was controlled around 190−195 °C. The thickness of all material was monitored using quartz crystal microbalance (QCM). Only for the perovskite active layer (CsBr:FAI:PbI_2 layer) deposition process, the substrate temperature was cooled down to 8 °C. After deposition of the perovskite active layer, both device and thin film were annealed at 135 °C for 30 min using a hot plate (YOTEC YS-200s). Finally, the perovskite device was encapsulated inside the nitrogen-filled glovebox under the oxygen (O_2) and moisture (H_2O) levels of <0.1 ppm using encapsulation glass cover to adhere a thin layer of UV-epoxy resin adhesive (Everwide EXC345). The encapsulated device was exposed to the UV curing lamp for 90 s to ensure the resin is cured. The UV curing lamp system (Heraeus Noblelight F300S) is connected to a power supply (Heraeus P300MT).

The electron energy spectrum of the perovskite film can be measured using ultraviolet photoelectron spectroscopy (UPS). The chemical composition of the perovskite film was obtained using X-ray photoelectron spectroscopy (XPS) and the data were processed using XPSPEAK software. The absorption coefficient spectra of the CsFAPbIBr perovskite film was obtained using a UV−vis spectrophotometer (JASCO V-770) and their thickness was measured using a surface profiler (Bruker Dektak XT). The X-ray diffraction (XRD) pattern was measured using XRD system (Bruker D2 PHASER XE-T edition). The perovskite film roughness was measured using atomic force microscopy (AFM) measurement (Bruker Innova AFM). All the perovskite film measurements mentioned above was carried out on a glass substrate except for the GIWAXS measurement (on a silicon wafer substrate). We conducted GISAXS and GIWAXS measurements simultaneously at the 23A beamline station of the National Synchrotron Radiation Research Center (NSRRC) in Taiwan. The incident monochromatic X-ray beam has a photon energy of 10 keV (wavelength of 1.2398 Å), and the incident angle to each film was aligned precisely to 0.2°. A flat-panel detector (pixel number of C10158DK is 2352) was used to collect the wide-angle scattering signals with a sample-to-detector distance of 19.5 cm, and the collection time for each measurement was 10 s. The reduced 1D GIWAXS profiles were obtained by radially cutting along the out-of-plane direction (defined as the Qz direction) normal to the film surface and the in-plane direction (defined as Qx direction) parallel to the film surface by using FIT2D program. The out-of-plane and in-plane 1D GIWAXS profiles (for the edge-on and face-on crystallites) were reduced, respectively, by taking radially sliced cake cuts (integration along the azimuthally polar angle (χ): 90−135°, polar angle (χ): 160−180°, assuming 1/2 circular symmetry) from the 2D GIWAXS pattern to include the diffraction spots from perovskite crystallites with different orientations. In the lifetime testing, the perovskite film was kept in the humidity-controlled dry cabinet (Eureka Drybox) at a temperature of 25 °C and a humidity level of 30%.

The perovskite device performance such as current density−voltage ($J-V$) characteristic under light conditions was measured using one sun solar simulator (Newport 91160A) with an intensity of 100 mW cm^{-2} connected with a source meter (Keithley 2636A). For the dark condition, the $J-V$ characteristic of the perovskite photodetector device was measured only using a source meter. The external quantum efficiency (EQE) spectrum, integral current density, and responsivity device were measured using a quantum efficiency (QE) measurement system (Enlitech QE-R) recorded in AC mode. The machine calibration was done beforehand using a silicon photodetector (Hamamatsu S1337). The noise current value was acquired using noise current frequency spectrum software developed by Enlitech (Enlitech PD-QE), which is connected to a source meter (Keithley 2636A). The linear dynamic range (LDR) measurement was performed utilizing a green light emitting diode (LED) (Thorlabs M530L3) at a wavelength of 530 nm as a light source, where a filter wheel (Thorlabs FW102CNEB) was used to control the light source intensity. The response at −3 dB, pulse response, and response time were measured using green LED illumination (Thorlabs LED525L) at wavelength 525 nm as the light source. The light source was connected to a function generator (Tektronix AFG3102C) to generate a square pulse where the LED power was set to 1 mW cm^{-2}. The perovskite device response output was amplified using a preamplifier (Signal Recovery Model 5182) multiplied by an A/V amplification factor of 10^{-6} then recorded using an oscilloscope (Teledyne Lecroy WaveRunner625Zi). The silicon photodetector (Newport 818-SL) was used as a baseline and comparison data for the perovskite device. The impedance and capacitance−voltage (C−V) characteristics of the perovskite device were measured using electrochemical impedance spectroscopy (Solartron Material Lab XM). The input AC signal oscillator was set to 50 mV and the given frequency sweep was tuned from 1 Hz to 1 MHz. The $C-V$ plot was obtained using a frequency of 1 kHz at a given voltage sweep from −2.5 to 2.5 V. For the lifetime testing, the perovskite device was kept exposed under one sun LED solar simulator (Newport LSH-7320). All the measurements above were done under room temperature conditions.

■ ASSOCIATED CONTENT

Supporting Information

The Supporting Information is available free of charge at https://pubs.acs.org/doi/10.1021/acsami.3c00839.

UPS curves of CsFAPbIBr perovskite films, perovskite device lifetime of EQE−current density−responsivity curves and $J-V$ under dark and light conditions, AFM image lifetimes of perovskite films, perovskite device performance lifetimes and their hysteresis indexes (PDF)

■ AUTHOR INFORMATION

Corresponding Authors

Shun-Wei Liu − *Organic Electronics Research Center and Department of Electronic Engineering, Ming Chi University of Technology, New Taipei City 24301, Taiwan;* orcid.org/0000-0002-3128-905X; Email: swliu@mail.mcut.edu.tw

Yu-Ching Huang − *Department of Materials Engineering, Ming Chi University of Technology, New Taipei City 24301, Taiwan;* orcid.org/0000-0003-4772-8050; Email: huangyc@mail.mcut.edu.tw

Authors

Nurul Ridho Al Amin − *Department of Electronic Engineering, National Taiwan University of Science and Technology, Taipei 10617, Taiwan; Organic Electronics Research Center, Ming Chi University of Technology, New Taipei City 24301, Taiwan;* orcid.org/0000-0002-7887-0271

Chih-Chien Lee − *Department of Electronic Engineering, National Taiwan University of Science and Technology, Taipei 10617, Taiwan*

Yu-Chen Huang − *Organic Electronics Research Center and Department of Materials Engineering, Ming Chi University of Technology, New Taipei City 24301, Taiwan*

Chun-Jen Shih − *Organic Electronics Research Center, Ming Chi University of Technology, New Taipei City 24301, Taiwan;* orcid.org/0000-0003-0861-7147

Richie Estrada − *Department of Electronic Engineering, National Taiwan University of Science and Technology, Taipei 10617, Taiwan; Organic Electronics Research Center, Ming Chi University of Technology, New Taipei City 24301, Taiwan;* orcid.org/0000-0003-1250-0320

https://doi.org/10.1021/acsami.3c00839
ACS Appl. Mater. Interfaces 2023, 15, 21284−21295

Sajal Biring − *Organic Electronics Research Center and Department of Electronic Engineering, Ming Chi University of Technology, New Taipei City 24301, Taiwan;* orcid.org/0000-0002-4442-1320

Meng-Hsueh Kuo − *Department of Electronic Engineering, National Taiwan University of Science and Technology, Taipei 10617, Taiwan; Organic Electronics Research Center, Ming Chi University of Technology, New Taipei City 24301, Taiwan*

Chia-Feng Li − *Department of Materials Engineering, Ming Chi University of Technology, New Taipei City 24301, Taiwan; Department of Materials Science and Engineering, National Taiwan University, Taipei 10617, Taiwan*

Complete contact information is available at: https://pubs.acs.org/10.1021/acsami.3c00839

Notes

The authors declare no competing financial interest.

■ ACKNOWLEDGMENTS

The authors acknowledge financial support from the National Science and Technology Council (Grant Nos. NSTC-111-2221-E-131-013, 111-2221-E-011-039-MY2, 111-2221-E-131-022, 109-2223-E-131-001-MY3). The corresponding author (S.-W. Liu) is grateful to Mr. H. H. Wu, Syskey Technology Co., Ltd. (Taiwan), for his assistance in designing the fabrication system. The corresponding author (Y.-C. Huang) thanks Dr. Cheng-Si Tsao for the helpful suggestion regarding GISAXS/GIWAXS measurement.

■ REFERENCES

(1) Zhou, X.; Yang, D.; Ma, D. Extremely Low Dark Current, High Responsivity, All-Polymer Photodetectors with Spectral Response from 300 Nm to 1000 Nm. *Adv. Opt. Mater.* **2015**, *3* (11), 1570−1576.

(2) Wang, P.; Liu, S.; Luo, W.; Fang, H.; Gong, F.; Guo, N.; Chen, Z.-G.; Zou, J.; Huang, Y.; Zhou, X.; Wang, J.; Chen, X.; Lu, W.; Xiu, F.; Hu, W. Arrayed Van Der Waals Broadband Detectors for Dual-Band Detection. *Adv. Mater.* **2017**, *29* (16), 1604439.

(3) Li, L.; Lou, Z.; Shen, G. Flexible Broadband Image Sensors with SnS Quantum Dots/Zn_2SnO_4 Nanowires Hybrid Nanostructures. *Adv. Funct. Mater.* **2018**, *28* (6), 1705389.

(4) Simone, G.; Dyson, M. J.; Meskers, S. C. J.; Janssen, R. A. J.; Gelinck, G. H. Organic Photodetectors and Their Application in Large Area and Flexible Image Sensors: The Role of Dark Current. *Adv. Funct. Mater.* **2020**, *30* (20), 1904205.

(5) Zimmerman, J. D.; Diev, V. V.; Hanson, K.; Lunt, R. R.; Yu, E. K.; Thompson, M. E.; Forrest, S. R. Porphyrin-Tape/C_{60} Organic Photodetectors with 6.5% External Quantum Efficiency in the Near Infrared. *Adv. Mater.* **2010**, *22* (25), 2780−2783.

(6) Guo, F.; Yang, B.; Yuan, Y.; Xiao, Z.; Dong, Q.; Bi, Y.; Huang, J. A Nanocomposite Ultraviolet Photodetector Based on Interfacial Trap-Controlled Charge Injection. *Nat. Nanotechnol.* **2012**, *7* (12), 798−802.

(7) Jansen-van Vuuren, R. D.; Armin, A.; Pandey, A. K.; Burn, P. L.; Meredith, P. Organic Photodiodes: The Future of Full Color Detection and Image Sensing. *Adv. Mater.* **2016**, *28* (24), 4766−4802.

(8) Lee, C.; Estrada, R.; Li, Y.; Biring, S.; Amin, N. R. Al; Li, M.; Liu, S.; Wong, K. Vacuum-Processed Small Molecule Organic Photodetectors with Low Dark Current Density and Strong Response to Near-Infrared Wavelength. *Adv. Opt. Mater.* **2020**, *8* (17), 2000519.

(9) Sutherland, B. R.; Johnston, A. K.; Ip, A. H.; Xu, J.; Adinolfi, V.; Kanjanaboos, P.; Sargent, E. H. Sensitive, Fast, and Stable Perovskite Photodetectors Exploiting Interface Engineering. *ACS Photonics* **2015**, *2* (8), 1117−1123.

(10) Kielar, M.; Dhez, O.; Pecastaings, G.; Curutchet, A.; Hirsch, L. Long-Term Stable Organic Photodetectors with Ultra Low Dark Currents for High Detectivity Applications. *Sci. Rep.* **2016**, *6* (1), 39201.

(11) Bao, C.; Yang, J.; Bai, S.; Xu, W.; Yan, Z.; Xu, Q.; Liu, J.; Zhang, W.; Gao, F. High Performance and Stable All-Inorganic Metal Halide Perovskite-Based Photodetectors for Optical Communication Applications. *Adv. Mater.* **2018**, *30* (38), 1803422.

(12) Huang, Z.; Carey, J. E.; Liu, M.; Guo, X.; Mazur, E.; Campbell, J. C. Microstructured Silicon Photodetector. *Appl. Phys. Lett.* **2006**, *89* (3), 033506.

(13) Zhang, A.; Kim, H.; Cheng, J.; Lo, Y.-H. Ultrahigh Responsivity Visible and Infrared Detection Using Silicon Nanowire Phototransistors. *Nano Lett.* **2010**, *10* (6), 2117−2120.

(14) Fuentes-Hernandez, C.; Chou, W.-F.; Khan, T. M.; Diniz, L.; Lukens, J.; Larrain, F. A.; Rodriguez-Toro, V. A.; Kippelen, B. Large-Area Low-Noise Flexible Organic Photodiodes for Detecting Faint Visible Light. *Science* **2020**, *370* (6517), 698−701.

(15) Saparov, B.; Mitzi, D. B. Organic−Inorganic Perovskites: Structural Versatility for Functional Materials Design. *Chem. Rev.* **2016**, *116* (7), 4558−4596.

(16) Adinolfi, V.; Ouellette, O.; Saidaminov, M. I.; Walters, G.; Abdelhady, A. L.; Bakr, O. M.; Sargent, E. H. Fast and Sensitive Solution-Processed Visible-Blind Perovskite UV Photodetectors. *Adv. Mater.* **2016**, *28* (33), 7264−7268.

(17) Hu, W.; Cong, H.; Huang, W.; Huang, Y.; Chen, L.; Pan, A.; Xue, C. Germanium/Perovskite Heterostructure for High-Performance and Broadband Photodetector from Visible to Infrared Telecommunication Band. *Light Sci. Appl.* **2019**, *8* (1), 106.

(18) Li, C.; Wang, H.; Wang, F.; Li, T.; Xu, M.; Wang, H.; Wang, Z.; Zhan, X.; Hu, W.; Shen, L. Ultrafast and Broadband Photodetectors Based on a Perovskite/Organic Bulk Heterojunction for Large-Dynamic-Range Imaging. *Light Sci. Appl.* **2020**, *9* (1), 31.

(19) Nguyen, T. M. H.; Kim, S.; Bark, C. W. Solution-Processed and Self-Powered Photodetector in Vertical Architecture Using Mixed-Halide Perovskite for Highly Sensitive UVC Detection. *J. Mater. Chem. A* **2021**, *9* (2), 1269−1276.

(20) Min, H.; Lee, D. Y.; Kim, J.; Kim, G.; Lee, K. S.; Kim, J.; Paik, M. J.; Kim, Y. K.; Kim, K. S.; Kim, M. G.; Shin, T. J.; Il Seok, S. Perovskite Solar Cells with Atomically Coherent Interlayers on SnO2 Electrodes. *Nature* **2021**, *598* (7881), 444−450.

(21) Li, N.; Feng, A.; Guo, X.; Wu, J.; Xie, S.; Lin, Q.; Jiang, X.; Liu, Y.; Chen, Z.; Tao, X. Engineering the Hole Extraction Interface Enables Single-Crystal $MAPbI_3$ Perovskite Solar Cells with Efficiency Exceeding 22% and Superior Indoor Response. *Adv. Energy Mater.* **2022**, *12* (7), 2103241.

(22) Ávila, J.; Momblona, C.; Boix, P. P.; Sessolo, M.; Bolink, H. J. Vapor-Deposited Perovskites: The Route to High-Performance Solar Cell Production? *Joule* **2017**, *1* (3), 431−442.

(23) Gil-Escrig, L.; Momblona, C.; La-Placa, M.-G.; Boix, P. P.; Sessolo, M.; Bolink, H. J. Vacuum Deposited Triple-Cation Mixed-Halide Perovskite Solar Cells. *Adv. Energy Mater.* **2018**, *8* (14), 1703506.

(24) Chiang, Y.-H.; Anaya, M.; Stranks, S. D. Multisource Vacuum Deposition of Methylammonium-Free Perovskite Solar Cells. *ACS Energy Lett.* **2020**, *5* (8), 2498−2504.

(25) Vaynzof, Y. The Future of Perovskite Photovoltaics—Thermal Evaporation or Solution Processing? *Adv. Energy Mater.* **2020**, *10* (48), 2003073.

(26) Kojima, A.; Teshima, K.; Shirai, Y.; Miyasaka, T. Organometal Halide Perovskites as Visible-Light Sensitizers for Photovoltaic Cells. *J. Am. Chem. Soc.* **2009**, *131* (17), 6050−6051.

(27) Liu, M.; Johnston, M. B.; Snaith, H. J. Efficient Planar Heterojunction Perovskite Solar Cells by Vapour Deposition. *Nature* **2013**, *501* (7467), 395−398.

(28) Lee, M. M.; Teuscher, J.; Miyasaka, T.; Murakami, T. N.; Snaith, H. J. Efficient Hybrid Solar Cells Based on Meso-Superstructured Organometal Halide Perovskites. *Science* **2012**, *338* (6107), 643−647.

(29) Hsiao, S.-Y.; Lin, H.-L.; Lee, W.-H.; Tsai, W.-L.; Chiang, K.-M.; Liao, W.-Y.; Ren-Wu, C.-Z.; Chen, C.-Y.; Lin, H.-W. Efficient All-Vacuum Deposited Perovskite Solar Cells by Controlling Reagent Partial Pressure in High Vacuum. *Adv. Mater.* **2016**, *28* (32), 7013−7019.
(30) Momblona, C.; Gil-Escrig, L.; Bandiello, E.; Hutter, E. M.; Sessolo, M.; Lederer, K.; Blochwitz-Nimoth, J.; Bolink, H. J. Efficient Vacuum Deposited P-i-n and n-i-p Perovskite Solar Cells Employing Doped Charge Transport Layers. *Energy Environ. Sci.* **2016**, *9* (11), 3456−3463.
(31) Li, J.; Wang, H.; Chin, X. Y.; Dewi, H. A.; Vergeer, K.; Goh, T. W.; Lim, J. W. M.; Lew, J. H.; Loh, K. P.; Soci, C.; Sum, T. C.; Bolink, H. J.; Mathews, N.; Mhaisalkar, S.; Bruno, A. Highly Efficient Thermally Co-Evaporated Perovskite Solar Cells and Mini-Modules. *Joule* **2020**, *4* (5), 1035−1053.
(32) Borchert, J.; Milot, R. L.; Patel, J. B.; Davies, C. L.; Wright, A. D.; Martínez Maestro, L.; Snaith, H. J.; Herz, L. M.; Johnston, M. B. Large-Area, Highly Uniform Evaporated Formamidinium Lead Triiodide Thin Films for Solar Cells. *ACS Energy Lett.* **2017**, *2* (12), 2799−2804.
(33) Li, T.; Pan, Y.; Wang, Z.; Xia, Y.; Chen, Y.; Huang, W. Additive Engineering for Highly Efficient Organic−Inorganic Halide Perovskite Solar Cells: Recent Advances and Perspectives. *J. Mater. Chem. A* **2017**, *5* (25), 12602−12652.
(34) Yi, C.; Luo, J.; Meloni, S.; Boziki, A.; Ashari-Astani, N.; Grätzel, C.; Zakeeruddin, S. M.; Röthlisberger, U.; Grätzel, M. Entropic Stabilization of Mixed A-Cation ABX $_3$ Metal Halide Perovskites for High Performance Perovskite Solar Cells. *Energy Environ. Sci.* **2016**, *9* (2), 656−662.
(35) Liu, T.; Lai, H.; Wan, X.; Zhang, X.; Liu, Y.; Chen, Y. Cesium Halides-Assisted Crystal Growth of Perovskite Films for Efficient Planar Heterojunction Solar Cells. *Chem. Mater.* **2018**, *30* (15), 5264−5271.
(36) Chen, C.-Y.; Tsao, C.-S.; Huang, Y.-C.; Liu, H.-W.; Chiu, W.-Y.; Chuang, C.-M.; Jeng, U.-S.; Su, C.-J.; Wu, W.-R.; Su, W.-F.; Wang, L. Mechanism and Control of the Structural Evolution of a Polymer Solar Cell from a Bulk Heterojunction to a Thermally Unstable Hierarchical Structure. *Nanoscale* **2013**, *5* (16), 7629.
(37) Schlipf, J.; Müller-Buschbaum, P. Structure of Organometal Halide Perovskite Films as Determined with Grazing-Incidence X-Ray Scattering Methods. *Adv. Energy Mater.* **2017**, *7* (16), 1700131.
(38) Oesinghaus, L.; Schlipf, J.; Giesbrecht, N.; Song, L.; Hu, Y.; Bein, T.; Docampo, P.; Müller-Buschbaum, P. Toward Tailored Film Morphologies: The Origin of Crystal Orientation in Hybrid Perovskite Thin Films. *Adv. Mater. Interfaces* **2016**, *3* (19), 1600403.
(39) Wu, W.-R.; Su, C.-J.; Chuang, W.-T.; Huang, Y.-C.; Yang, P.-W.; Lin, P.-C.; Chen, C.-Y.; Yang, T.-Y.; Su, A.-C.; Wei, K.-H.; Liu, C.-M.; Jeng, U.-S. Surface Layering and Supersaturation for Top-Down Nanostructural Development during Spin Coating of Polymer/Fullerene Thin Films. *Adv. Energy Mater.* **2017**, *7* (14), 1601842.
(40) Huang, Y.-C.; Liu, W.-S.; Tsao, C.-S.; Wang, L. Mechanistic Insights into the Effect of Polymer Regioregularity on the Thermal Stability of Polymer Solar Cells. *ACS Appl. Mater. Interfaces* **2019**, *11* (43), 40310−40319.
(41) Fu, S.; Li, X.; Wan, J.; Zhang, W.; Song, W.; Fang, J. In Situ Stabilized CsPbI $_3$ for Air-Fabricated Inverted Inorganic Perovskite Photovoltaics with Wide Humidity Operating Window. *Adv. Funct. Mater.* **2022**, *32* (14), 2111116.
(42) Reus, M. A.; Reb, L. K.; Weinzierl, A. F.; Weindl, C. L.; Guo, R.; Xiao, T.; Schwartzkopf, M.; Chumakov, A.; Roth, S. V.; Müller-Buschbaum, P. Time-Resolved Orientation and Phase Analysis of Lead Halide Perovskite Film Annealing Probed by In Situ GIWAXS. *Adv. Opt. Mater.* **2022**, *10* (14), 2102722.
(43) Kuo, K.-H.; Estrada, R.; Lee, C.-C.; Al Amin, N. R.; Li, Y.-Z.; Hadiyanto, M. Y.; Liu, S.-W.; Wong, K.-T. A New Dioxasilepine−Aryldiamine Hybrid Electron-Blocking Material for Wide Linear Dynamic Range and Fast Response Organic Photodetector. *ACS Appl. Mater. Interfaces* **2022**, *14* (16), 18782−18793.
(44) Xiao, K.; Tu, B.; Chen, L.; Heil, T.; Wen, L.; Jiang, L.; Antonietti, M. Photo-Driven Ion Transport for a Photodetector Based on an Asymmetric Carbon Nitride Nanotube Membrane. *Angew. Chemie Int. Ed.* **2019**, *58* (36), 12574−12579.
(45) Hadiyanto, M. Y.; Estrada, R.; Lee, C.-C.; Biring, S.; Akbar, A. K.; Li, C.-Y.; Shih, C.-J.; Li, Y.-Z.; Liu, S.-W. Transparent Photodetectors with Ultra-Low Dark Current and High Photoresponse for near-Infrared Detection. *Org. Electron.* **2021**, *99*, 106356.
(46) Shieh, W.; Djordjevic, I. Optical Communication Fundamentals. In *OFDM for Optical Communications*; Elsevier, 2010; pp 53−118.
(47) Bunge, C.-A.; Beckers, M.; Lustermann, B. Basic Principles of Optical Fibres. In *Polymer Optical Fibres*; Elsevier, 2017; pp 47−118.
(48) Zhang, M.; Zhang, F.; Wang, Y.; Zhu, L.; Hu, Y.; Lou, Z.; Hou, Y.; Teng, F. High-Performance Photodiode-Type Photodetectors Based on Polycrystalline Formamidinium Lead Iodide Perovskite Thin Films. *Sci. Rep.* **2018**, *8* (1), 11157.
(49) Kim, H.-S.; Park, N.-G. Parameters Affecting $I - V$ Hysteresis of CH $_3$ NH $_3$ PbI $_3$ Perovskite Solar Cells: Effects of Perovskite Crystal Size and Mesoporous TiO $_2$ Layer. *J. Phys. Chem. Lett.* **2014**, *5* (17), 2927−2934.
(50) Sanchez, R. S.; Gonzalez-Pedro, V.; Lee, J.-W.; Park, N.-G.; Kang, Y. S.; Mora-Sero, I.; Bisquert, J. Slow Dynamic Processes in Lead Halide Perovskite Solar Cells. Characteristic Times and Hysteresis. *J. Phys. Chem. Lett.* **2014**, *5* (13), 2357−2363.
(51) Rong, Y.; Hu, Y.; Ravishankar, S.; Liu, H.; Hou, X.; Sheng, Y.; Mei, A.; Wang, Q.; Li, D.; Xu, M.; Bisquert, J.; Han, H. Tunable Hysteresis Effect for Perovskite Solar Cells. *Energy Environ. Sci.* **2017**, *10* (11), 2383−2391.
(52) Liu, P.; Wang, W.; Liu, S.; Yang, H.; Shao, Z. Fundamental Understanding of Photocurrent Hysteresis in Perovskite Solar Cells. *Adv. Energy Mater.* **2019**, *9* (13), 1803017.
(53) Li, S.; Tong, S.; Yang, J.; Xia, H.; Zhang, C.; Zhang, C.; Shen, J.; Xiao, S.; He, J.; Gao, Y.; Yang, B.; Meng, J.-Q. High-Performance Formamidinium-Based Perovskite Photodetectors Fabricated via Doctor-Blading Deposition in Ambient Condition. *Org. Electron.* **2017**, *47*, 102−107.
(54) Han, Q.; Bae, S.; Sun, P.; Hsieh, Y.; Yang, Y.; Rim, Y. S.; Zhao, H.; Chen, Q.; Shi, W.; Li, G.; Yang, Y. Single Crystal Formamidinium Lead Iodide (FAPbI $_3$): Insight into the Structural, Optical, and Electrical Properties. *Adv. Mater.* **2016**, *28* (11), 2253−2258.
(55) Bao, C.; Xu, W.; Yang, J.; Bai, S.; Teng, P.; Yang, Y.; Wang, J.; Zhao, N.; Zhang, W.; Huang, W.; Gao, F. Bidirectional Optical Signal Transmission between Two Identical Devices Using Perovskite Diodes. *Nat. Electron.* **2020**, *3* (3), 156−164.
(56) Chen, G.; Qiu, Y.; Gao, H.; Zhao, Y.; Feng, J.; Jiang, L.; Wu, Y. Air-Stable Highly Crystalline Formamidinium Perovskite 1D Structures for Ultrasensitive Photodetectors. *Adv. Funct. Mater.* **2020**, *30* (14), 1908894.
(57) Yu, D.; Cao, F.; Gu, Y.; Han, Z.; Liu, J.; Huang, B.; Xu, X.; Zeng, H. Broadband and Sensitive Two-Dimensional Halide Perovskite Photodetector for Full-Spectrum Underwater Optical Communication. *Nano Res.* **2021**, *14* (4), 1210−1217.
(58) Yu, D.; Cao, F.; Shen, Y.; Liu, X.; Zhu, Y.; Zeng, H. Dimensionality and Interface Engineering of 2D Homologous Perovskites for Boosted Charge-Carrier Transport and Photodetection Performances. *J. Phys. Chem. Lett.* **2017**, *8* (12), 2565−2572.
(59) Zhang, F.; Yang, B.; Zheng, K.; Yang, S.; Li, Y.; Deng, W.; He, R. Formamidinium Lead Bromide (FAPbBr3) Perovskite Microcrystals for Sensitive and Fast Photodetectors. *Nano-Micro Lett.* **2018**, *10* (3), 43.
(60) Pan, R.; Li, H.; Wang, J.; Jin, X.; Li, Q.; Wu, Z.; Gou, J.; Jiang, Y.; Song, Y. High-Responsivity Photodetectors Based on Formamidinium Lead Halide Perovskite Quantum Dot-Graphene Hybrid. *Part. Part. Syst. Charact.* **2018**, *35* (4), 1700304.
(61) Liang, F.-X.; Wang, J.-Z.; Zhang, Z.-X.; Wang, Y.-Y.; Gao, Y.; Luo, L.-B. Broadband, Ultrafast, Self-Driven Photodetector Based on

https://doi.org/10.1021/acsami.3c00839
ACS Appl. Mater. Interfaces 2023, 15, 21284−21295

Cs-Doped FAPbI $_3$ Perovskite Thin Film. *Adv. Opt. Mater.* **2017**, *5* (22), 1700654.
(62) Ma, S.; Jang, G.; Kim, S.; Kwon, H.-C.; Goh, S.; Ban, H.; Cho, J. H.; Moon, J. Multifunctional Self-Combustion Additives Strategy to Fabricate Highly Responsive Hybrid Perovskite Photodetectors. *ACS Appl. Mater. Interfaces* **2020**, *12* (37), 41674−41686.
(63) Zhang, Z.-X.; Zeng, L.-H.; Tong, X.-W.; Gao, Y.; Xie, C.; Tsang, Y. H.; Luo, L.-B.; Wu, Y.-C. Ultrafast, Self-Driven, and Air-Stable Photodetectors Based on Multilayer PtSe $_2$ /Perovskite Heterojunctions. *J. Phys. Chem. Lett.* **2018**, *9* (6), 1185−1194.
(64) Zeng, L.; Chen, Q.; Zhang, Z.; Wu, D.; Yuan, H.; Li, Y.; Qarony, W.; Lau, S. P.; Luo, L.; Tsang, Y. H. Multilayered PdSe $_2$ /Perovskite Schottky Junction for Fast, Self-Powered, Polarization-Sensitive, Broadband Photodetectors, and Image Sensor Application. *Adv. Sci.* **2019**, *6* (19), 1901134.
(65) Wang, Y.; Zhang, X.; Wang, D.; Li, X.; Meng, J.; You, J.; Yin, Z.; Wu, J. Compositional Engineering of Mixed-Cation Lead Mixed-Halide Perovskites for High-Performance Photodetectors. *ACS Appl. Mater. Interfaces* **2019**, *11* (31), 28005−28012.
(66) Zhou, H.; Song, Z.; Wang, C.; Grice, C. R.; Song, Z.; Zhao, D.; Wang, H.; Yan, Y. Double Coating for the Enhancement of the Performance in a MA $_{0.7}$ FA $_{0.3}$ PbBr $_3$ Photodetector. *ACS Photonics* **2018**, *5* (6), 2100−2105.
(67) Adams, G. R.; Eze, V. O.; Shohag, M. A. S.; Simpson, R.; Parker, H.; Okoli, O. I. Fabrication of Rapid Response Self-Powered Photodetector Using Solution-Processed Triple Cation Lead-Halide Perovskite. *Eng. Res. Express* **2020**, *2* (1), 015043.
(68) Wang, W.; Zhao, D.; Zhang, F.; Li, L.; Du, M.; Wang, C.; Yu, Y.; Huang, Q.; Zhang, M.; Li, L.; Miao, J.; Lou, Z.; Shen, G.; Fang, Y.; Yan, Y. Highly Sensitive Low-Bandgap Perovskite Photodetectors with Response from Ultraviolet to the Near-Infrared Region. *Adv. Funct. Mater.* **2017**, *27* (42), 1703953.
(69) Wang, T.; Zheng, D.; Zhang, J.; Qiao, J.; Min, C.; Yuan, X.; Somekh, M.; Feng, F. High-Performance and Stable Plasmonic-Functionalized Formamidinium-Based Quasi-2D Perovskite Photodetector for Potential Application in Optical Communication. *Adv. Funct. Mater.* **2022**, *32* (48), 2208694.
(70) Kato, M.; Fujiseki, T.; Miyadera, T.; Sugita, T.; Fujimoto, S.; Tamakoshi, M.; Chikamatsu, M.; Fujiwara, H. Universal Rules for Visible-Light Absorption in Hybrid Perovskite Materials. *J. Appl. Phys.* **2017**, *121* (11), 115501.
(71) Koech, R. K.; Ichwani, R.; Martin, J. L.; Oyewole, D. O.; Oyelade, O. V.; Olanrewaju, Y. A.; Sanni, D. M.; Adeniji, S. A.; Grimm, R. L.; Bello, A.; Oyewole, O. K.; Ntsoenzok, E.; Soboyejo, W. O. A Study of the Effects of a Thermally Evaporated Nanoscale CsBr Layer on the Optoelectronic Properties and Stability of Formamidinium-Rich Perovskite Solar Cells. *AIP Adv.* **2021**, *11* (9), 095112.
(72) Guerrero, A.; Garcia-Belmonte, G.; Mora-Sero, I.; Bisquert, J.; Kang, Y. S.; Jacobsson, T. J.; Correa-Baena, J.-P.; Hagfeldt, A. Properties of Contact and Bulk Impedances in Hybrid Lead Halide Perovskite Solar Cells Including Inductive Loop Elements. *J. Phys. Chem. C* **2016**, *120* (15), 8023−8032.
(73) Almora, O.; Aranda, C.; Mas-Marzá, E.; Garcia-Belmonte, G. On Mott-Schottky Analysis Interpretation of Capacitance Measurements in Organometal Perovskite Solar Cells. *Appl. Phys. Lett.* **2016**, *109* (17), 173903.
(74) Hailegnaw, B.; Sariciftci, N. S.; Scharber, M. C. Impedance Spectroscopy of Perovskite Solar Cells: Studying the Dynamics of Charge Carriers Before and After Continuous Operation. *Phys. status solidi* **2020**, *217* (22), 2000291.
(75) Yadav, P.; Prochowicz, D.; Saliba, M.; Boix, P.; Zakeeruddin, S.; Grätzel, M. Interfacial Kinetics of Efficient Perovskite Solar Cells. *Crystals* **2017**, *7* (8), 252.
(76) von Hauff, E.; Klotz, D. Impedance Spectroscopy for Perovskite Solar Cells: Characterisation, Analysis, and Diagnosis. *J. Mater. Chem. C* **2022**, *10* (2), 742−761.

https://doi.org/10.1021/acsami.3c00839
ACS Appl. Mater. Interfaces 2023, 15, 21284−21295